Pressure-Driven Semiconductor-to-Metal, Magnetic, and Structural Transitions in the Ferrimagnetic Semiconductor $Mn_3Si_2Te_6$

Jun Hou[1,2†], Hanming Ma[1,2†], Qiangwei Yin[1,2†], Xiutong Deng[1,2], Pengfei Shan[1,2], Zhaorong Yang[4], Yoshiya Uwatoko[5], Xiaohui Yu[1,2], Xiaoli Ma[1], Youguo Shi[1,2], Xiaoli Dong[1,2], Hechang Lei[3*], Jianping Sun[1,2*], and Jinguang Cheng[1,2*]

[1]*Beijing National Laboratory for Condensed Matter Physics and Institute of Physics, Chinese Academy of Sciences, Beijing 100190, China*
[2]*School of Physical Sciences, University of Chinese Academy of Sciences, Beijing 100190, China*
[3]*School of Physics, Key Laboratory of Quantum State Construction and Manipulation (Ministry of Education), and Beijing Key Laboratory of Opto-electronic Functional Materials & Micro-nano Devices, Renmin University of China, Beijing 100872, China*
[4]*Anhui Province Key Laboratory of Condensed Matter Physics at Extreme Conditions, High Magnetic Field Laboratory, Chinese Academy of Sciences, Hefei 230031, China*
[5]*Institute for Solid State Physics, University of Tokyo, Kashiwa, Chiba 277-8581, Japan*

(Received 24 March 2025; accepted manuscript online 11 April 2025)

$Mn_3Si_2Te_6$ is a ferrimagnetic nodal-line semiconductor with colossal angular magnetoresistance at ambient pressure. In this work, we investigated the effect of hydrostatic pressure on its electrical transport properties, magnetic transition, and crystal structure by measuring resistivity, DC and AC magnetic susceptibility, and XRD under various pressures up to ∼20 GPa. Our results confirmed the occurrence of pressure-induced structural transition at $P_c \approx 10$–12 GPa accompanied by a concurrent drop of room-temperature resistance in $Mn_3Si_2Te_6$. In the low-pressure phase at $P < P_c$, the ferrimagnetic transition temperature T_c increases linearly with pressure from ∼75 K at ambient pressure to ∼257 K at 10.8 GPa, and the semiconducting state is converted gradually to a metallic behavior at $T < T_c$. Accurate structural information in the low-pressure phase has been extracted from refinements of single-crystal XRD data, which help us to understand the dramatic enhancement T_c. In the high-pressure phase at $P > P_c$, the sample exhibits a metallic behavior in the whole temperature range and its resistivity exhibits a kink anomaly at T_M, characteristic of critical scattering around a magnetic transition. Recovery of the Raman spectrum upon decompression indicated that pressure-induced structural transition is reversible without amorphization under hydrostatic pressure conditions. Our present work not only resolves some existing controversial issues but also provides new insights into pressure-driven diverse behaviors of $Mn_3Si_2Te_6$.

DOI: 10.1088/0256-307X/42/5/057403 CSTR: 32039.14.0256-307X.42.5.057403

1. Introduction. In recent years, the two-dimensional magnetic van der Waals (vdW) materials have received considerable attention because they exhibit many exotic physical properties and potential applications in spintronic devices.[1–11] Tuning the spin states by means of external stimuli such as magnetic field or high pressure, a variety of novel magneto-transport phenomena can be realized in the magnetic vdW materials,[12–17] such as CrX_3 (X = Cl, Br, and I),[18–20] Cr(Si/Ge)Te_3[21–23] and Fe_3GeTe_2.[24–26] Thus, much effort has been devoted to exploring novel vdW magnetic materials and associated intriguing physical phenomena.

As a three-dimensional analog of $Cr_2(Si/Ge)_2Te_6$, $Mn_3Si_2Te_6$ synthesized almost 40 years ago[27,28] was recently found to exhibit record-high values of colossal angular magnetoresistance (MR) as a ferrimagnetic (FIM) nodal-line semiconductor.[29] As shown in Fig. 1(a), $Mn_3Si_2Te_6$ adopts a self-intercalated vdW structure, consisting of alternatively stacked $Mn_2Si_2Te_6$ layers with the hexagonal honeycomb network of Mn1 atoms and the Mn layers with the triangular lattice of Mn2 atoms along the c axis. The $Mn1Te_6$ octahedra shares edges within the $Mn_2Si_2Te_6$ layers, which are then interconnected with each other via face-shared $Mn2Te_6$ octahedra. As highlighted in Fig. 1(b), such an arrangement produces three distinct Mn–Mn connections, i.e., d_1, d_2, and d_3 for face-, edge-, and corner-sharing $MnTe_6$ octahedra. Neutron diffraction experiments have established a FIM order below $T_c \approx 78$ K due to the antiparallel alignment of Mn1 and Mn2 spins with easy-plane anisotropy.[30] This FIM transition is manifested as a strong enhancement of magnetization below T_c. The resistivity of $Mn_3Si_2Te_6$ crystal exhibits an overall

†These authors contributed equally to this work.
*Corresponding author. Email: hlei@ruc.edu.cn; jpsun@iphy.ac.cn; jgcheng@iphy.ac.cn
© 2025 Chinese Physical Society and IOP Publishing Ltd. All rights, including for text and data mining, AI training, and similar technologies, are reserved.

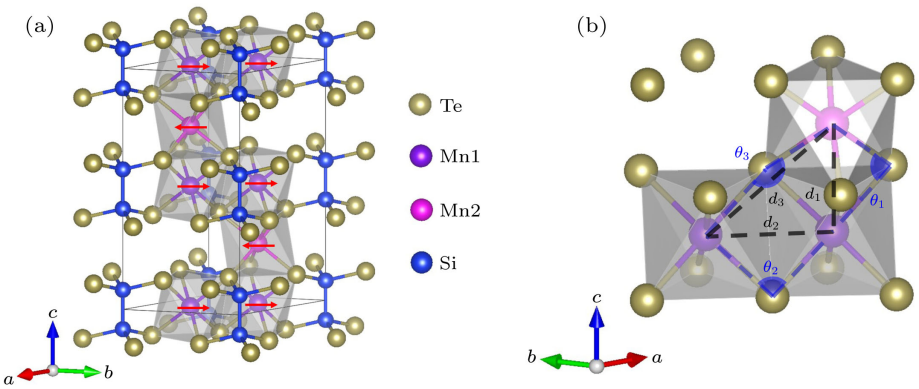

Fig. 1. (a) Crystal structure of $Mn_3Si_2Te_6$. The arrows represent the direction of Mn magnetic moment below T_c. (b) The Mn–Mn bond distance and Mn-Te-Mn bond angle for the neighboring Mn–Mn exchange interactions.

semiconducting behavior with a pronounced cusp-like anomaly at the FIM transition, followed by a quick upturn at low temperatures.[30–32] When the external field was applied along the hard c-axis, colossal angular MR up to 10^{11}%/rad appears at low temperatures, which has been attributed to the magnetic field-driven insulator-metal transition due to the lifting of nodal-line band degeneracy near the Fermi level.[29,32,33]

Since the magneto-transport properties of $Mn_3Si_2Te_6$ are extremely sensitive to the topological band structure and spin arrangements, the application of high pressure has been considered as an effective knob to regulate the electronic structures and to tip the balance of competing magnetic interactions. Recently, there are two independent high-pressure studies on the $Mn_3Si_2Te_6$ single crystals by using diamond anvil cell (DAC) technique.[34,35] Both studies have revealed a significant enhancement of T_c with a linear slope of $dT_c/dP \sim$ 14–16 K/GPa and pressure-induced structural transition at $P_c \sim$ 12–14 GPa. In addition, pressure-driven metallization and reduction of MR were also evidenced in both studies. Except for these common observations, however, there remain many discrepancies in the experimental results of these two studies. For example, in the report by Wang *et al.*,[34] pressure-induced metallization takes place at rather low pressures of ∼2.5 GPa, decoupled from the structural transition at $P_c \approx$ 12 GPa, which has been attributed to pressure-induced irreversible amorphization since the Raman modes were found to all disappear above P_c. In addition, the resistivity of high-pressure phase exhibits a rather weak temperature dependence without discernable anomalies indicative of any phase transition. In contrast, in the report by Susilo *et al.*,[35] pressure-induced metallization occurs concomitantly with the structural transition at $P_c \approx$ 14 GPa, and the high-pressure phase remains crystallized with a possible $C2/c$ symmetry and changes to another FIM state with easy-axis anisotropy along the c-direction. Although the FIM transition temperature T_c has been traced from the measurements of anomalous Hall effect, no anomaly can be observed in the resistivity of the metallic phase above P_c.[34] These discrepancies about the transport properties of $Mn_3Si_2Te_6$ crystals should be largely attributed to the non-hydrostatic pressure conditions in DAC employing solid pressure medium. This effect is more severe considering the layered structure of $Mn_3Si_2Te_6$.

To resolve these discrepancies, here we re-investigated the effect of hydrostatic pressure on the transport, magnetic, and structural properties of $Mn_3Si_2Te_6$ crystals by using the piston cylinder cell (PCC) and cubic anvil cell (CAC), both employing liquid pressure transmitting medium (PTM). Our results confirmed a linear enhancement of T_c from ∼75 K at ambient pressure to ∼257 K at 10.8 GPa and pressure-induced reversible structural transition without amorphization at $P_c \sim$ 10–12 GPa in $Mn_3Si_2Te_6$. Under improved hydrostatic pressure condition, we find that pressure-induced metallization occurs gradually above 3 GPa in the low-pressure phase and the metallic resistivity in the high-pressure phase displays a clear kink-like anomaly at T_M, characteristic of critical scattering around a magnetic transition. In addition, through refinements of single-crystal XRD (SXRD) data below P_c, we provide accurate structural information that is useful for quantitative analyses of competing magnetic interactions and understanding of the enhancement of T_c under pressure in $Mn_3Si_2Te_6$.

2. Experimental Details. $Mn_3Si_2Te_6$ single crystals used in the present study were synthesized via self-flux methods in vacuum sealed quartz tube as described in Ref. [36]. We employed the standard four-probe method to measure resistivity at ambient and high pressures. To avoid reaction between the measured sample and the silver paste, we first deposited four gold (Au) pads on the $Mn_3Si_2Te_6$ single crystals with magnetron sputtering apparatus and then attach the gold wires to these pads with 4929N silver paste. We have measured three pieces of $Mn_3Si_2Te_6$ samples (labeled as S1–S3) under various high pressures by using PCC for S1 up to 2.4 GPa and CAC for S2/S3 up to 12 GPa. The AC magnetic susceptibility of $Mn_3Si_2Te_6$ sample together with a piece of Pb as the pressure marker placed in the same coil was measured by using the mutual induction method. The excitation current is ∼1 mA with a frequency of 1117 Hz, and the output signal was picked up with a Stanford Research SR830 lock-in amplifier. The pressure values inside PCC and CAC were estimated by superconducting transition temperature of Pb with the formula P (GPa) $= [7.2 - T_c(P)]/0.365$. For these high-pressure measurements, the samples were im-

mersed in the liquid PTM (glycerol) to ensure an excellent hydrostatic pressure condition.

High-pressure DC magnetic susceptibility has also been measured by using a miniature BeCu PCC under various pressures up to 0.97 GPa in the commercial Magnetic Property Measurement System (MPMS-III, Quantum Design). The $Mn_3Si_2Te_6$ single crystal and a piece of Pb were loaded into a Teflon capsule filled with Daphne 7373 as the PTM, and the pressure values were monitored by the relative shift of the T_c of Pb. To reduce the contribution from the cell background, here all the measurements were performed in the zero-field-cooled (ZFC) mode.

High-pressure powder XRD data were collected at the BL15U1 station of the Shanghai Synchrotron Radiation Facility by using symmetric DAC filled with 4:1 methanol/ethanol mixture as PTM. SXRD measurements under high pressures were carried out with Xta LAB (Rigaku) AFC11 (RCD3): quarter-chi single diffractometer. The sample with the size of 300 μm × 80 μm was placed in a Re gasket hole of DAC filled with 4:1 methanol/ethanol mixture. The pressures in DAC were monitored at room temperature with the ruby fluorescence method.

3. Results and Discussion. Figure 2 shows the temperature dependence of in-plane resistivity $\rho(T)$ and its derivative $d\rho/dT$ of $Mn_3Si_2Te_6$ under various hydrostatic pressures up to 2.35 GPa in PCC and 12 GPa in CAC. At ambient pressure, the $\rho(T)$ first increases upon cooling down from room temperature, exhibiting the typical semiconducting behavior, and then displays a clear cusp-like anomaly at $T_c \approx 75$ K, producing a metallic regime down to ∼45 K due to the suppression of spin fluctuations in the FIM ordered state, followed by a quick upturn at low temperatures, as shown in Fig. 2(a). Here, we determined the FIM transition temperature T_c from the sharp peak of $d\rho/dT$ as shown in Fig. 2(b). The above results at ambient pressure are consistent with previous reports.[30–32,34,35] When the external pressure was applied gradually, the $\rho(T)$ of $Mn_3Si_2Te_6$ is reduced monotonically in the measured temperature range and the cusp-like anomaly at T_c shifts to higher temperature progressively. In particular, the resistivity upturn below 30 K is quickly suppressed, and the metallic region is expanded accordingly. A fully metallic state is eventually achieved above 9 GPa. Meanwhile, the anomaly in $\rho(T)$ is also much weakened at pressures of 10.8 and 11.7 GPa, signaling the modification of the electronic ground state in this system.

By monitoring the peaks of $d\rho/dT$, we can track the evolutions with pressure of $T_c(P)$. As shown in Figs. 2(b) and 2(d), T_c increases with pressure from ∼75 K at ambient pressure to ∼235 K at 9 GPa. Interestingly, at 10.8 GPa, two successive anomalies were observed at ∼220 K and 257 K. The latter anomaly should be ascribed to the FIM transition as the lower pressures, while the former should be attributed to the emergence of a new magnetic transition. This conjecture is confirmed by observing a similar anomaly at ∼130 K under 11.7–12 GPa, as shown in the top of Fig. 2(d). It seems that the $\rho(T)$ at 10.8 GPa is located at the phase boundary with the coexistence of two phases, the low-pressure phase with a FIM transition at T_c and a high-pressure phase with a transition at T_M. Since the nature of transition at higher pressures above 10.8 GPa is unclear, here we denote it as T_M to distinguish it from T_c of the low-pressure phase. In comparison with the previous high-pressure studies with DAC, the resistivity anomaly at T_c is much clearer and the emergent phase transition at T_M can be well resolved, demonstrating the merits of high-pressure measurements under hydrostatic pressure conditions.

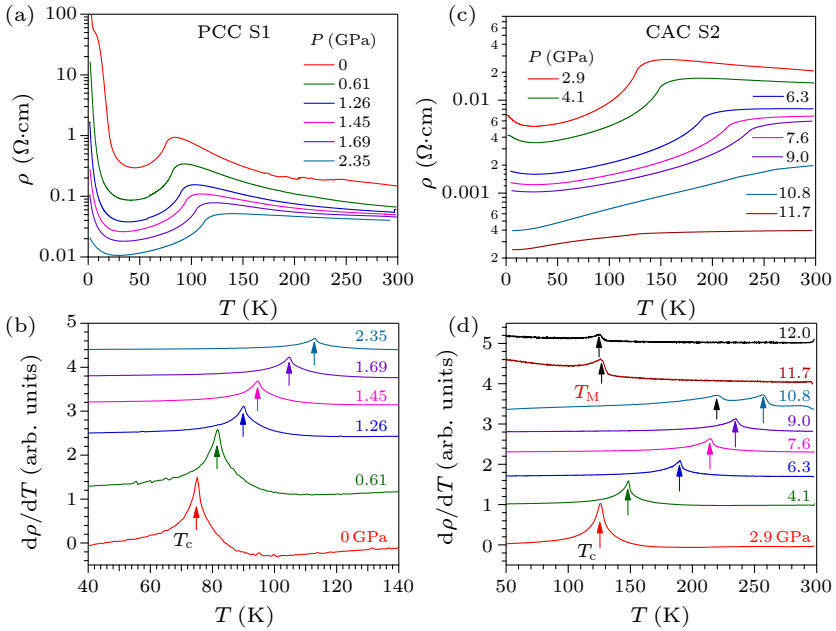

Fig. 2. Temperature dependence of in-plane resistivity $\rho(T)$ and its derivative $d\rho/dT$ for the $Mn_3Si_2Te_6$ single crystals under various high pressures from S1 in PCC up to 2.35 GPa in (a) and (b), and for S2 in CAC up to 12 GPa in (c) and (d).

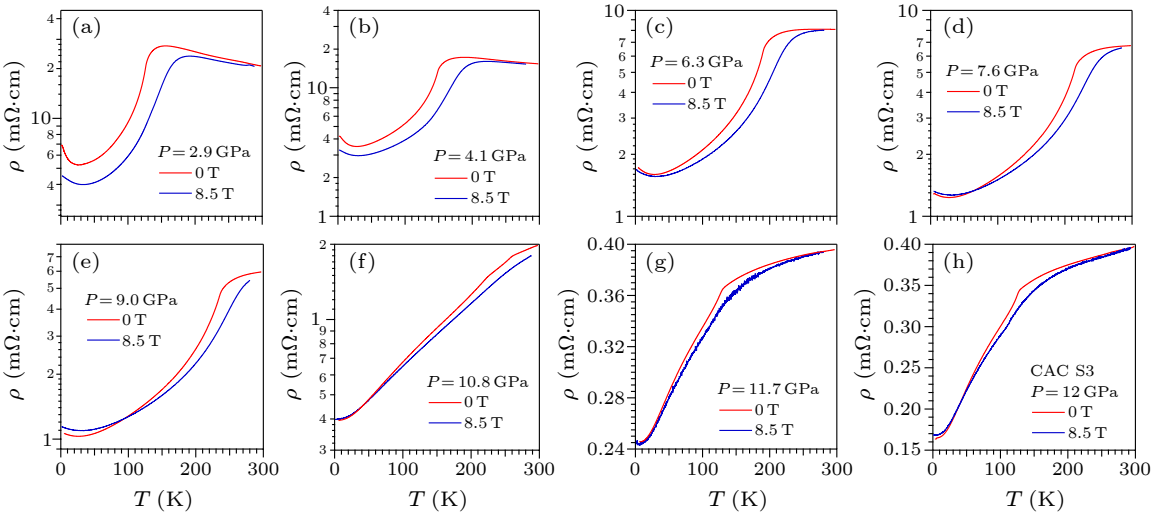

Fig. 3. Temperature dependence of in-plane resistivity of $Mn_3Si_2Te_6$ single crystal under 0 and 8.5 T at each measured pressure.

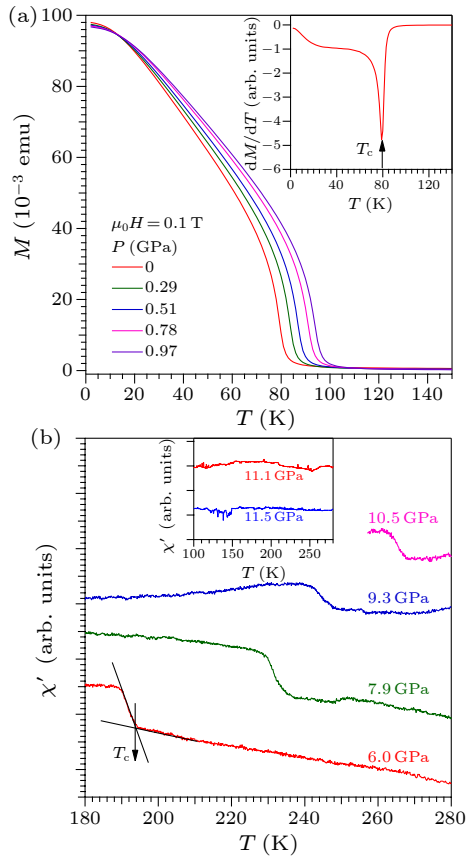

Fig. 4. Temperature dependence of (a) DC magnetization $M(T)$ up to 0.97 GPa measured in PCC and (b) AC magnetic susceptibility $\chi'(T)$ up to 11.5 GPa in CAC.

To examine the evolution of MR under pressure, we also measured $\rho(T)$ of $Mn_3Si_2Te_6$ (S2 and S3) at 8.5 T under various pressures up to 12 GPa in CAC. Figure 3 shows the $\rho(T)$ data at 0 and 8.5 T at each pressure. At 2.9 GPa, the sharp semiconductor-to-metal transition in $\rho(T)$ moves from ∼125 K at 0 T to ∼180 K at 8.5 T, showing a pronounced negative MR in Fig. 3(a). However, the MR exhibits a large reduction both at T_c and low temperatures compared to that at ambient pressure. With increasing pressure to 4.1 GPa, the sharp drop of $\rho(T)$ at T_c is still clear and T_c is shifted from ∼150 K at 0 T to ∼190 K at 8.5 T as shown in Fig. 3(b), accompanying further reduction of MR. Upon increasing pressure to 7.6 and 9.0 GPa, the T_c exhibits similar enhancement from 0 to 8.5 T, but the negative MR is observed mainly around the FIM with the appearance of positive MR at low temperatures in Figs. 3(d) and 3(e). At 10.8 GPa, both the anomaly of $\rho(T)$ at T_c and the MR are much diminished, except for the region near T_c in Fig. 3(f). On the other hand, the $\rho(T)$ at ∼12 GPa displays an obvious kink at T_M ∼ 125 K at 0 T, which is smoothed out at 8.5 T, producing moderate negative MR around T_M. These observations are reproducible as shown in Fig. 3(h) for another sample S3 at 12 GPa. The kink-like anomaly and negative MR at T_M at ∼12 GPa is similar to that observed in the itinerant ferromagnet such as $SrRuO_3$,[37] indicting the magnetic origin of this emergent transition in the high-pressure phase.

Since the electrical transport properties of $Mn_3Si_2Te_6$ are strongly coupled with the magnetic transition, we further tracked the evolution of magnetic transition as a function of pressure by measuring the DC and AC magnetic susceptibility in PCC and CAC. Figure 4(a) displays the DC $M(T)$ curves measured under ZFC mode at 0.1 T up to 0.97 GPa. As can be seen, the FIM transition is gradually shifted to high temperatures with increasing pressure. Here, we have determined T_c^M from the dip of dM/dT, as shown in the inset of Fig. 4(a). The step-like anomaly in the AC $\chi'(T)$ can be used to further track T_c up to at least 10.5 GPa. Here, we defined T_c as the intersection of two straight lines as shown in Fig. 4(b). At 10.5 GPa, T_c reaches ∼270 K, which is consistent with the resistivity data shown in Fig. 2. However, at higher pressures 11.1 and 11.5 GPa, corresponding to emergence of T_M in resistivity measurements, no obvious anomaly can be found in the $\chi'(T)$, as shown in inset of Fig. 4(b).

Based on the above resistivity and magnetic measurements under high pressures, we construct the T–P phase diagram of $Mn_3Si_2Te_6$. As shown in Fig. 5(a),

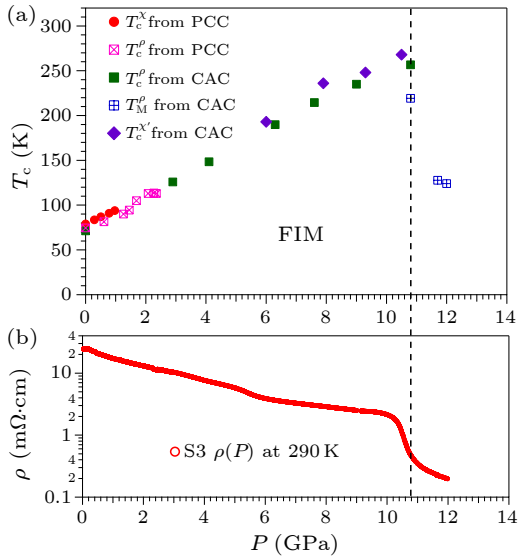

Fig. 5. (a) Pressure dependencies of the transition temperatures T_c and T_M determined from the $\rho(T)$, $M(T)$, and $\chi'(T)$ measurements. (b) Pressure dependence of resistivity $\rho(P)$ measured at room temperature for sample S3.

$T_c(P)$ increases linearly with pressure at a slope of $\sim$ 17 K/GPa, reaching about 257 K at 10.8 GPa, above which the FIM order experiences a sudden modification into another new state featured by a lower characteristic temperature $T_M \sim 125$ K at $\sim$12 GPa. The coexistence of two transitions at 10.8 GPa indicates a first-order nature for the pressure-driven phase transition, which is also reflected from the sudden drop of the resistivity $\rho(P)$ measured at room temperature for sample S3 shown in Fig. 5(b). In addition, we also noted a weak anomaly in the $\rho(P)$ curve at $\sim$6 GPa, which should be attributed to the solidification of the liquid PTM upon compression at room temperature.

To verify pressure-induced structure phase transition, we first performed high-pressure synchrotron XRD measurements on the pulverized $Mn_3Si_2Te_6$ samples and presented the obtained powder XRD pattens in Fig. 6(a). As can be seen clearly, the diffraction peaks experience an abrupt change at $\sim$10 GPa, especially the significant shift of the main peak, signaling the occurrence of structure phase transition. However, the XRD patterns above 10 GPa cannot be described by any of the structural models, $P6_3/mmc$, $CmCm$, $C2/m$, and $C2/c$ proposed in Ref. [35]. The relatively limited diffraction peaks in the powder XRD data prevent us solving the structure of the high-pressure phase. To overcome this issue, we resorted to SXRD measurements under high pressure. As shown in Fig. 6(b), we successfully collected the SXRD patterns up to $\sim$10 GPa, above which the data quality becomes worse due to deformation of crystals so that it prevents us determining directly the high-pressure structure. Nevertheless, the high-quality SXRD data allow us to extract the atomic positions and thus detailed structure information, including the lattice parameters, bond lengths and angles, which are collected in Tables 1 and 2.

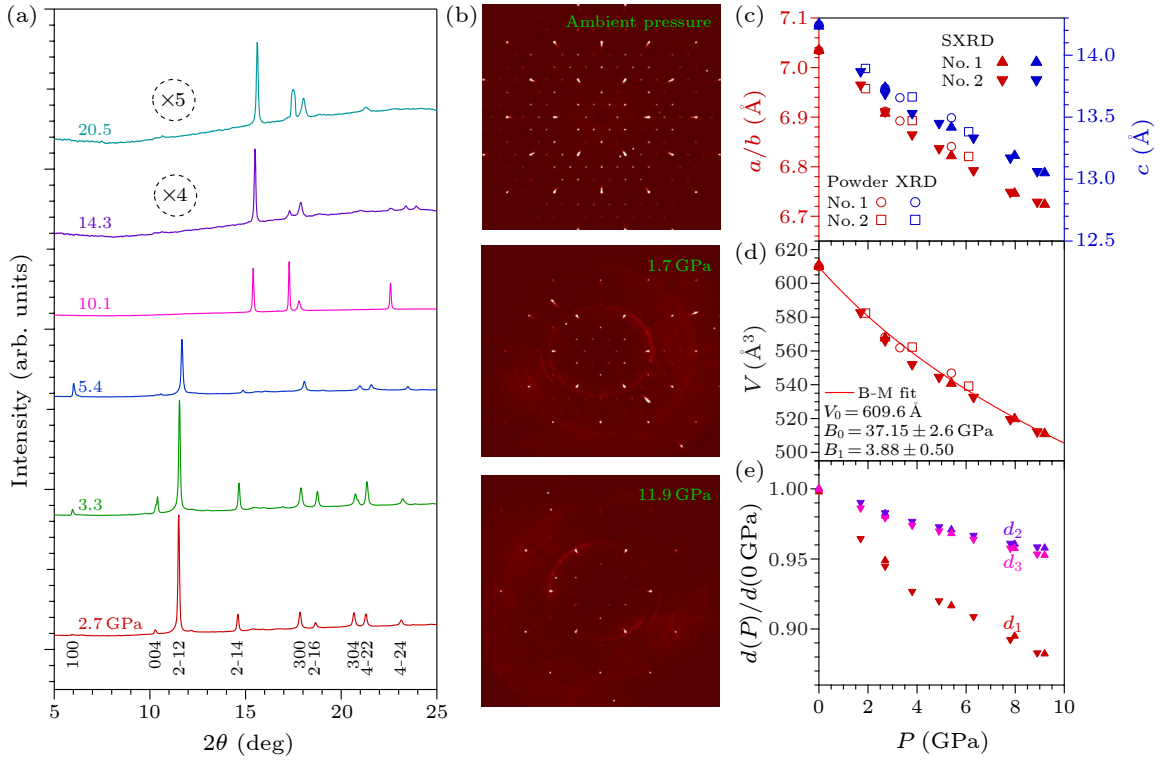

Fig. 6. Structure evolution of $Mn_3Si_2Te_6$ under high pressures. (a) The high-pressure synchrotron XRD patterns of pulverized $Mn_3Si_2Te_6$ under various pressures up to 20.5 GPa. (b) SXRD patterns at ambient pressure, 1.7, and 11.9 GPa. (c) and (d) Pressure dependences of lattice parameters a, c, and volume V. The solid line in (d) represents the fitting to $V(P)$ by using the Birch–Murnaghan equation. (e) Pressure dependence of the normalized neighboring Mn–Mn bond d_1, d_2, and d_3.

Table 1. Lattice parameters and atomic positions of $Mn_3Si_2Te_6$ at high pressure.

Pressure (GPa)	a/b (Å)	c (Å)	$Mn1_z$	Si_z	Te_x, y, z
			No. 1		
0_outside DAC	7.035(1)	14.253(3)	0.5007(4)	0.581(1)	1.0035(2), 0.6588(2), 0.6278(2)
0_inside DAC	7.034(3)	14.23(11)	0.501(4)	0.582(9)	1.0037(6), 0.6586(6), 0.6274(16)
2.7	6.907(7)	13.74(2)	0.505(3)	0.583(7)	1.0118(6), 0.6604(6), 0.6311(12)
5.4	6.821(4)	13.41(9)	0.507(3)	0.585(5)	1.0165(7), 0.6611(5), 0.6332(8)
8.0	6.746(3)	13.19(8)	0.509(3)	0.586(6)	1.0196(8), 0.6613(5), 0.6348(8)
9.2	6.724(3)	13.05(9)	0.510(5)	0.586(9)	1.0205(15), 0.6614(9), 0.6354(16)
			No. 2		
1.7	6.965(1)	13.86(1)	0.503(4)	0.582(9)	1.0097(8), 0.6600(9), 0.6305(15)
2.7	6.911(1)	13.69(2)	0.505(7)	0.586(16)	1.012(2), 0.660(2), 0.631(3)
3.8	6.865(1)	13.53(1)	0.507(5)	0.582(12)	1.014(2), 0.661(1), 0.632(2)
4.9	6.837(1)	13.45(1)	0.507(8)	0.581(17)	1.017(2), 0.661(3), 0.633(3)
6.3	6.792(1)	13.33(1)	0.508(5)	0.585(11)	1.018(2), 0.661(1), 0.635(2)
7.8	6.748(1)	13.17(1)	0.509(5)	0.584(12)	1.020(2), 0.661(1), 0.635(2)
8.9	6.729(1)	13.06(1)	0.510(8)	0.586(16)	1.020(3), 0.661(2), 0.636(3)

[a]Space groups: P-31c; Mn1: $4f(2/3, 1/3, z)$, Mn2: $2c(2/3, 1/3, 3/4)$, Si: $4e(1, 1, z)$, and Te: $12i(x, y, z)$.

Table 2. Selected Mn–Mn bond distances and Mn–Te–Mn bond angles.

Pressure (GPa)	d_1 (Å)	d_2 (Å)	d_3 (Å)	θ_1 (deg)	θ_2 (deg)	θ_3 (deg)
			No. 1			
0_outside DAC	3.5533(6)	4.06188(6)	5.4101(4)	74.628(10)	87.257(8)	135.531(7)
0_inside DAC	3.546(7)	4.06134(19)	5.408(5)	74.52(10)	87.48(7)	135.59(4)
2.7	3.372(7)	3.9901(5)	5.305(5)	71.89(11)	87.20(8)	135.85(4)
5.4	3.257(5)	3.9435(5)	5.238(4)	70.22(8)	87.17(4)	135.96(2)
8.0	3.180(5)	3.9019(6)	5.180(3)	69.25(8)	87.05(4)	136.050(18)
9.2	3.135(7)	3.8906(9)	5.154(5)	68.56(12)	87.24(7)	135.97(3)
			No. 2			
1.7	3.427(7)	4.0221(5)	5.336(5)	72.53(11)	87.30(7)	135.69(4)
2.7	3.357(11)	3.9922(8)	5.298(7)	71.63(17)	87.16(11)	135.75(7)
3.8	3.293(8)	3.9674(7)	5.269(5)	70.72(12)	87.28(8)	135.79(5)
4.9	3.269(12)	3.9517(12)	5.247(8)	70.29(19)	87.12(11)	135.94(6)
6.3	3.229(8)	3.9270(9)	5.215(5)	69.82(12)	86.88(8)	135.93(4)
7.8	3.171(8)	3.9040(10)	5.181(5)	69.05(12)	87.15(8)	136.01(4)
8.9	3.137(12)	3.8932(15)	5.158(8)	68.60(19)	87.13(12)	135.99(6)

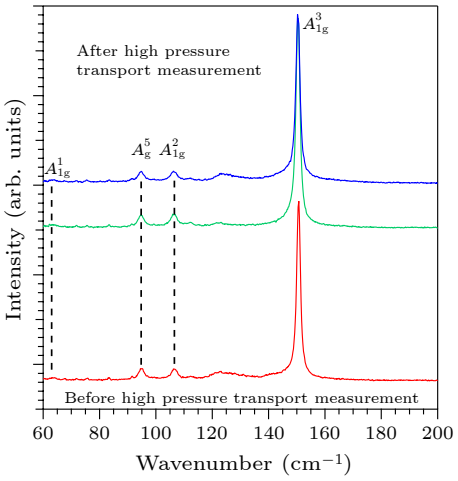

Fig. 7. Raman spectra of single crystal $Mn_3Si_2Te_6$ before and after highpressure measurements.

Figures 6(c) and 6(d) displays the pressure-dependent lattice parameters a, c, and volume V obtained from the refinements of above high-pressure powder XRD and SXRD data in the trigonal structure below 10 GPa. As expected, c-axis shows a larger compressibility than a-axis in the layered structure, i.e., c-axis is reduced by 8.45% whereas a-axis reduced by 4.42% at 9.2 GPa. The continuous shrinkage of volume $V(P)$ can be well fitted by the Birch-Murnaghan equation,[38,39] which gives the volume $V_0 = 609.6$ Å^3 and the bulk modulus $B_0 = 37.15$ GPa.

To gain more insights into the pressure-induced dramatic enhancement of T_c in the low-pressure phase, we plotted in Fig. 6(e) the pressure dependence of the neighboring Mn–Mn bond distances up to 9.2 GPa. As can be seen, the d_1 decreases by 11.7%, while d_2 and d_3 decrease merely about 4.2% and 4.7%, respectively. According to the theoretical calculations,[30] the magnetic ground state is determined by the first three exchange coupling, i.e., J_1 for the nearest-neighbor face-sharing Mn–Mn sites along the c-axis, J_2 for the nearest-neighbor edge-sharing Mn–Mn sites in the ab-plane, and J_3 for the corner-sharing Mn–Mn sites across the layers, which are all antiferromagnetic exchange interactions. The FIM ground state comes from the competition of these three interactions. Consid-

ering the monotonic reduction of Mn–Mn bond lengths, all three exchange interactions are expected to be enhanced upon compression. It is expected that the dominant J_1 should increase stronger than J_2 and J_3, thus favors the FIM ground state instead of competing antiferromagnetic state and greatly enhance FIM T_c. This detailed structural information should benefit a quantitative description of the pressure dependence of T_c.

To further confirm the recovery of structure phase transition, we measured the Raman spectra of sample S3 after finishing all the transport measurements, as displayed in Fig. 7. The Raman spectra before and after the high-pressure transport measurements show the same features, which indicates that the structure phase transition is reversible in the measured pressure range below 12 GPa.

4. Conclusion. In summary, our present study on $Mn_3Si_2Te_6$ single crystals under hydrostatic pressures confirmed a linear enhancement of the FIM transition temperature with a slope of $dT_c/dP \sim 17$ K/GPa up to 10.8 GPa, above which a structural transition takes place, resulting in a new magnetic phase with a characteristic transition temperature $T_M \sim 120$ K at 12 GPa. Detailed structural information from the refinement of SXRD helps us to understand the evolution of FIM in the low-pressure phase. But the crystal structure of the high-pressure phase remains unsolved in the present study, which would require a better resolution of SXRD data above 14 GPa.

Acknowledgments. This work was supported by the National Key R&D Program of China (Grant Nos. 2023YFA1406100, 2022YFA1403900, 2024YFA1408400, 2021YFA1400200, 2022YFA1403800, and 2023YFA1406500), the National Natural Science Foundation of China (Grant Nos. 12174424, 12025408, 11921004, U22A6005, and 12274459), the Youth Innovation Promotion Association of Chinese Academy of Sciences (Grant No. 2023007), and the Chinese Academy of Sciences President's International Fellowship Initiative (Grant No. 2024PG0003). Part of the work was supported by the Center for Materials Genome and the Synergetic Extreme Condition User Facility (SECUF, https://cstr.cn/31123.02.SECUF). High-pressure synchrotron XRD measurements were performed at the BL15U1 station of Shanghai Synchrotron Radiation Facility.

References

[1] Jiang J, Xu L, Qiu C, and Peng L M 2023 *Nature* **616** 470

[2] Oh S H, Altug H, Jin X, Low T, Koester S J, Ivanov A P, Edel J B, Avouris P, and Strano M S 2021 *Nat. Commun.* **12** 3824

[3] Vizner Stern M, Waschitz Y, Cao W, Nevo I, Watanabe K, Taniguchi T, Sela E, Urbakh M, Hod O, and Ben Shalom M 2021 *Science* **372** 1462

[4] Wang G, Dai Z, Xiao J, Feng S, Weng C, Liu L, Xu Z, Huang R, and Zhang Z 2019 *Phys. Rev. Lett.* **123** 116101

[5] Novoselov K S, Mishchenko A, Carvalho A, and Castro Neto A H 2016 *Science* **353** aac9439

[6] Lan G B, Xu H J, Zhang Y, Cheng C, He B, Li J H, He C L, Wan C H, Feng J F, and Wei H X 2023 *Chin. Phys. Lett.* **40** 058501

[7] Wang G Y, Yang K, Ma Y Z H, Liu L, Lu D, Zhou Y X, and Wu H 2023 *Chin. Phys. Lett.* **40** 077301

[8] Dong X L, Jia X, Yan Z, Shen X M, Li Z Y, Qiao Z H, and Xu X H 2023 *Chin. Phys. Lett.* **40** 087301

[9] Guo D P, Wang C, Wang L J, Lu Y H, Wu H, Zhang Y N, and Ji W 2024 *Chin. Phys. Lett.* **41** 047501

[10] Meng K, Li Z Y, Shen Y C, Bi X Y, Rao J H, Qian Y T, Gao Z S, Chen P, Qiu C Y, Qin F 2024 *Chin. Phys. Lett.* **41** 097501

[11] Li Q, Zhen W L, Wang N, Shi M, Yu Y, Pan S Y, Deng L, Cai J Q, Wang K, Zou L K 2024 *Chin. Phys. Lett.* **41** 107503

[12] Vijayvargia A, Zhang H, Barros K, Lin S Z, and Erten O 2025 *Phys. Rev. B* **111** 094404

[13] Diederich G M, Cenker J, Ren Y, Fonseca J, Chica D G, Bae Y J, Zhu X, Roy X, Cao T, Xiao D, and Xu X 2023 *Nat. Nanotechnol.* **18** 23

[14] Song T, Fei Z, Yankowitz M, Lin Z, Jiang Q, Hwangbo K, Zhang Q, Sun B, Taniguchi T, Watanabe K, McGuire M A, Graf D, Cao T, Chu J H, Cobden D H, Dean C R, Xiao D, and Xu X 2019 *Nat. Mater.* **18** 1298

[15] Li T, Jiang S, Sivadas N, Wang Z, Xu Y, Weber D, Goldberger J E, Watanabe K, Taniguchi T, Fennie C J, Fai Mak K, and Shan J 2019 *Nat. Mater.* **18** 1303

[16] Jiang S, Shan J, and Mak K F 2018 *Nat. Mater.* **17** 406

[17] Jiang S, Li L, Wang Z, Mak K F, and Shan J 2018 *Nat. Nanotechnol.* **13** 549

[18] Sarkar S and Kratzer P 2021 *Phys. Rev. B* **103** 224421

[19] Xue F, Hou Y, Wang Z, and Wu R 2019 *Phys. Rev. B* **100** 224429

[20] Bacaksiz C, Šabani D, Menezes R M, and Milošević M V 2021 *Phys. Rev. B* **103** 125418

[21] Kang S, Kang S, Kim H S, and Yu J 2023 *npj 2D Mater. Appl.* **7** 13

[22] Musfeldt J L, Mandrus D G, and Liu Z 2023 *npj 2D Mater. Appl.* **7** 28

[23] Lin M W, Zhuang H L, Yan J, Ward T Z, Puretzky A A, Rouleau C M, Gai Z, Liang L, Meunier V, Sumpter B G, Ganesh P, Kent P R C, Geohegan D B, Mandrus D G, and Xiao K 2016 *J. Mater. Chem. C* **4** 315

[24] Fei Z, Huang B, Malinowski P, Wang W, Song T, Sanchez J, Yao W, Xiao D, Zhu X, May A F, Wu W, Cobden D H, Chu J H, and Xu X 2018 *Nat. Mater.* **17** 778

[25] Zha H M, Li W, Zhang G J, Liu W J, Deng L W, Jiang Q, Ye M, Wu H, Chang H X, and Qiao S 2023 *Chin. Phys. Lett.* **40** 087501

[26] Wang Z A, Zhang X M, Zhu W K, Yan F G, Liu P F, Yuan Z, and Wang K Y 2023 *Chin. Phys. Lett.* **40** 077201

[27] VIincent H, Leroux D, Bijaoui D, Riment R, and Schlenker C 1986 *J. Solid State Chem.* **63** 349

[28] Rimet R, Schlenker C, and Vincent H 1981 *J. Magn. Magn. Mater.* **25** 7

[29] Seo J, De C, Ha H, Lee J E, Park S, Park J, Skourski Y, Choi E S, Kim B, Cho G Y, Yeom H W, Cheong S W, Kim J H, Yang B J, Kim K, and Kim J S 2021 *Nature* **599** 576

[30] May A F, Liu Y, Calder S, Parker D S, Pandey T, Cakmak E, Cao H, Yan J, and McGuire M A 2017 *Phys. Rev. B* **95** 174440

[31] Liu Y, Hu Z, Abeykoon M, Stavitski E, Attenkofer K, Bauer E D, and Petrovic C 2021 *Phys. Rev. B* **103** 245122

[32] Ni Y, Zhao H, Zhang Y, Hu B, Kimchi I, and Cao G 2021 *Phys. Rev. B* **103** L161105

[33] Zhang Y, Ni Y, Zhao H, Hakani S, Ye F, DeLong L, Kimchi I, and Cao G 2022 *Nature* **611** 467

[34] Wang J, Wang S, He X, Zhou Y, An C, Zhang M, Zhou Y, Han Y, Chen X, Zhou J, and Yang Z 2022 *Phys. Rev. B* **106** 045106

[35] Susilo R A, Kwon C I, Lee Y, Salke N P, De C, Seo J, Kang B, Hemley R J, Dalladay-Simpson P, Wang Z, Kim D Y, Kim K, Cheong S W, Yeom H W, Kim K H, and Kim J S 2024 *Nat. Commun.* **15** 3998
[36] Wu Q, Yin Q, Zhang S, Hu T, Wu D, Yue L, Li B, Xu S, Li R, Liu Q, Lei H, Dong T, and Wang N 2024 *Adv. Optical Mater.* **12** 2301863
[37] Allen P B, Berger H, Chauvet O, Forro L, Jarlborg T, Junod A, Revaz B, and Santi G 1996 *Phys. Rev. B* **53** 4393
[38] Birch F 1947 *Phys. Rev.* **71** 809
[39] Murnaghan F D 1937 *Am. J. Math.* **59** 517